

# 3D Soft Metamaterials with Negative Poisson's Ratio

Sahab Babaee, Jongmin Shim, James C. Weaver, Elizabeth R. Chen, Nikita Patel, and Katia Bertoldi\*

When materials are uniaxially compressed, they typically expand in directions orthogonal to the applied load. Here, we exploit buckling to design a new class of three dimensional metamaterials with negative Poisson's ratio that contract in the transverse direction under compressive loading regimes. These proposed metamaterials consist of an array of patterned elastomeric spherical shells, which due to a mechanical instability, undergo a significant isotropic volume reduction when deformed. The large geometric non-linearities introduced in the system by buckling are exploited to achieve a negative Poisson's ratio and retain this unusual property over a wide range of applied deformations. Here, we identify a library of auxetic building blocks and define procedures to guide their selection and assembly. The auxetic properties of these materials are demonstrated both through experimental and finite element simulation approaches and exhibit excellent qualitative and quantitative agreement. As a result of this unusual behavior, these proposed metamaterials could be useful for the design of protective and energy absorbing materials, efficient membrane filters with variable permeability, and acoustic dampeners.

Metamaterials are rationally designed artificial materials which gain their properties from structure rather than composition. Since it was first shown that microstructures built from non-magnetic conducting sheets can exhibit effective magnetic permeability,<sup>[1]</sup> the metamaterial concept has been quickly extended to photonic,<sup>[2]</sup> acoustic<sup>[3]</sup> and mechanical,<sup>[4]</sup> systems, leading to the design of a variety of materials with properties not previously thought possible.

The Poisson's ratio defines the ratio between the transverse and axial strain.<sup>[5]</sup> Materials that are uniaxially compressed

typically expand in the directions orthogonal to the applied load. Counter-intuitively, materials with a negative Poisson's ratio (auxetic materials) contract in the transverse direction.<sup>[6,7]</sup> The first reported example of an artificial auxetic material was a foam with re-entrant cells that unfolded when stretched.<sup>[8]</sup> Since then, several periodic 2D geometries and mechanisms have been suggested to achieve a negative Poisson's ratio.<sup>[9]</sup> While auxetic responses have been demonstrated in many crystals,<sup>[10]</sup> very few designs of synthetic 3D auxetic materials have been proposed.<sup>[4]</sup> Analytical studies have identified 3D auxetic systems consisting of networks of beams,<sup>[11]</sup> multipods<sup>[12]</sup> and rigid units,<sup>[13]</sup> and only very recently, a metallic 3D architecture based on a bow-tie functional element has been fabricated.<sup>[14]</sup> In all of these systems, however, the auxetic behavior is exhibited only in the limit of small strains, and the design of 3D auxetic systems capable of retaining these unusual properties at large strains still remains a challenge.<sup>[4]</sup>

The design of metamaterials capable of responding reversibly to changes in their environment is of fundamental importance for the development of the next generation of actuators and sensors, tunable optics and smart responsive surfaces.<sup>[15,16]</sup> Furthermore, a remarkable feature of responsive metamaterials is that any of their properties can be switched or fine-tuned just by applying a stimulus to alter their initial architecture.

In order to successfully design a new class of 3D auxetic materials capable of retaining this unusual response over a wide range of applied strains, we exploited the large geometric non-linearities introduced in the system by instabilities. Through a combination of desktop-scale experiments and finite element (FE) simulations, we investigated the auxetic responses of these structures, finding excellent qualitative and quantitative agreement. Since the 3D auxetic behavior is induced by elastic buckling, we have named these new materials "Bucklicrystals". We believe that these Bucklicrystals open new design avenues for the construction of 3D auxetic materials over a wide range of length scales.

We began by recognizing that a structural unit capable of isotropic volume reduction represents the ideal building block to construct 3D auxetic metamaterials whose response can be controlled by the application of a stimulus. Such responses have been recently demonstrated for patterned spherical shells,<sup>[17]</sup> where a significant change in volume has been observed as a result of an elastic instability. The hole arrangement on the spherical shell has also been explored, showing that only five patterns comprising of 6, 12, 24, 30 and 60 holes are possible for such building blocks.<sup>[17]</sup> Note that these five spherical structures can be classified into two symmetry groups: the shells with 6, 12 and 24 holes have octahedral symmetry, while those with 30 and 60 holes have icosahedral symmetry.

S. Babaee,<sup>[†]</sup> Dr. E. R. Chen, N. Patel, Prof. K. Bertoldi  
School of Engineering and Applied Sciences  
Harvard University  
Cambridge, MA 02138, USA  
E-mail: bertoldi@seas.harvard.edu  
Prof. J. Shim<sup>[†]</sup>



Department of Civil, Structural and Environmental Engineering  
University at Buffalo  
Buffalo, NY 14260, USA

Dr. J. C. Weaver  
Wyss Institute for Biologically Inspired Engineering  
Harvard University  
Boston, MA 02115, USA  
Prof. K. Bertoldi  
Kavli Institute for Bionano Science and Technology  
Harvard University  
Cambridge, MA 02138, USA

<sup>[†]</sup>These authors contributed equally to this work.

DOI: 10.1002/adma.201301986

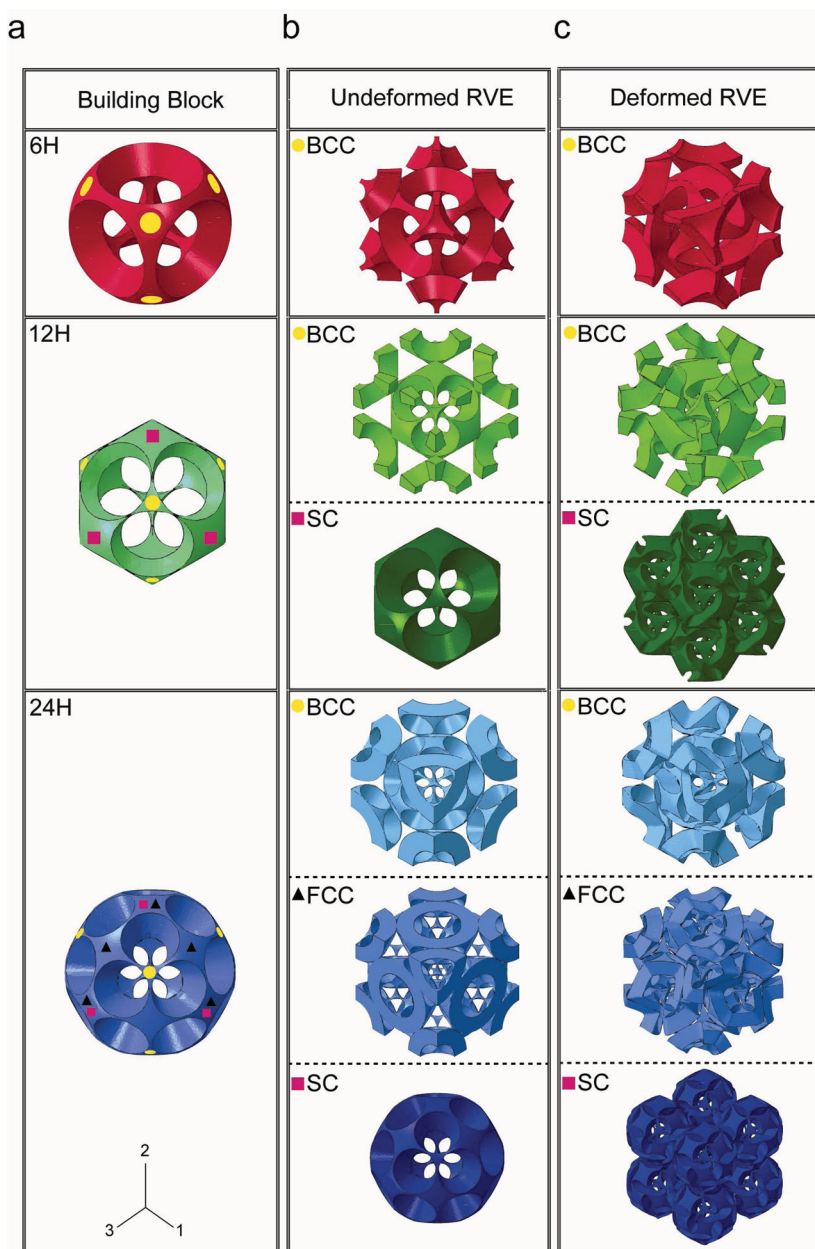


**Figure 1.** Gallery of Bucklicrystals. a) Building blocks with 6, 12 and 24 holes. For the sake of simplicity, we always color the building blocks with 6, 12 and 24 holes with red, green and blue, respectively. Moreover, we also identify the junctions where the building blocks are attached to the surrounding units using yellow circles, black triangles, and magenta squares for *bcc*, *fcc*, and *sc* packing configurations, respectively. b) Representative volume elements (RVE) for the Bucklicrystal in the undeformed configuration. c) Buckled configurations for the RVEs under uniaxial compression.

Having identified the building blocks, we then defined procedures to guide their assembly. Here, we focused on cubic crystal systems (i.e. simple cubic (*sc*), body-centered cubic (*bcc*), and face-centered cubic (*fcc*)) because of their simplicity and highest symmetry order out of the seven lattice systems. Since we required that both the building blocks and the metamaterial have octahedral symmetry, only spherical shells with 6, 12 and 24 holes were considered in this study (Figures 1a and S1).

Furthermore, for the sake of simplicity and ease of scalability, we constructed each metamaterial from a single type of building block.

Since each building block has a limited number of sites where adjacent building blocks can be attached to each other (see markers in Figure 1a) and metamaterials with octahedral symmetry can be built only via connecting identical junctions (i.e. junctions identified by the same type of markers in Figure 1a), only six different Bucklicrystals can be built (Figures 1b and S2): *bcc* crystals using building blocks with 6, 12 and 24 holes, *sc* crystals using building blocks with 12 and 24 holes, and *fcc* crystal using building blocks with 24 holes. Having identified all possible configurations for the Bucklicrystals, we next investigated their response through a combination of experiments and numerical simulations.

We first fabricated and mechanically tested a Bucklicrystal consisting of a *bcc* array of building blocks with 6 holes. Using additive manufacturing for the fabrication of individual molds for each unit cell, we fabricated the building blocks from a soft silicone-based rubber (vinyl polysiloxane with Young's modulus,  $E = 784$  KPa). The geometry of the building block comprises a spherical shell (inner diameter  $d_i = 19.8$  mm and wall thickness  $t = 7.1$  mm) that is patterned with a regular array of 6 circular voids that are slightly tapered (22 mm and 13 mm maximum and minimum diameter, respectively - Figures 1 and S1). Ninety one identical building blocks were fabricated and subsequently joined to form a *bcc* crystal using the same polymer as an adhesive agent.

The Bucklicrystal was then tested under uniaxial compression and the evolution of the microstructure was monitored taking tomographic images at five different levels of the applied nominal strain (calculated as change of height of the sample divided by the original height),  $\epsilon_{22}^{\text{applied}} = -0.03, -0.08, -0.15, -0.20, -0.30$ , with a micro-CT X-ray scanner (HMXST225, X-Tek). Figure 2 shows isometric and mid-cross sectional views of the structure in the undeformed ( $\epsilon_{22}^{\text{applied}} = 0$  - Figure 2a) and deformed ( $\epsilon_{22}^{\text{applied}} = -0.20$  - Figure 2b) configurations. Furthermore, a sequence

of progressively deformed shapes of the inner-most building block at different levels of strain is shown in Figure 2c. These snapshots clearly demonstrate that structural transformations induced by instabilities occur when the Bucklicrystal is compressed. All the building blocks are found to shrink significantly in all directions and their initially circular holes on the spherical shell transform into elongated, almost closed ellipses. Moreover, Figures 2a,b clearly show that all of the lateral boundaries of the

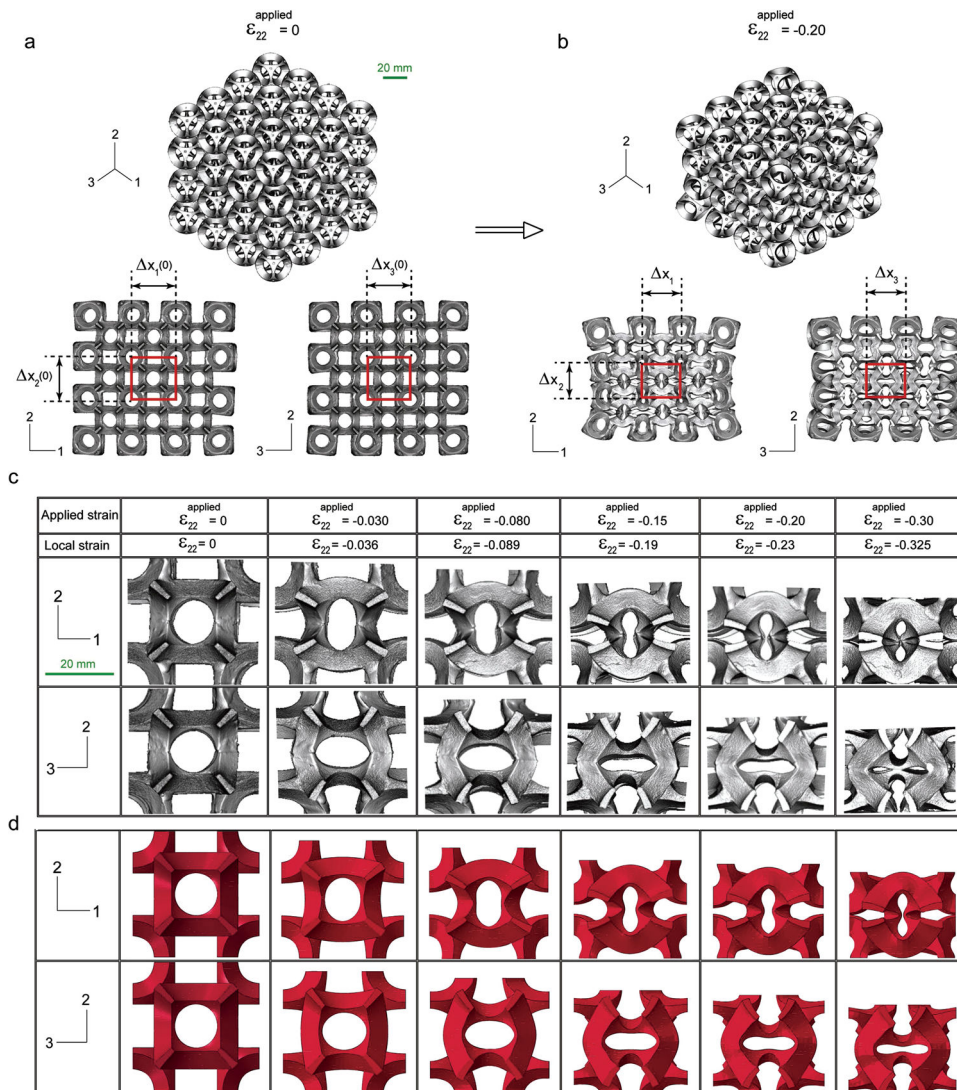


**Figure 2.** Experimental (micro-CT) and numerical images of the 6-hole Bucklicrystal. a) Isometric and cross-sectional views of the undeformed crystal from micro-CT X-ray imaging machine. b) Isometric and cross-sectional views of the uniaxially compressed crystal ( $\epsilon_{22}^{\text{applied}} = -0.20$ ) from micro-CT volumetric data sets. In the cross sectional views, the inner-most RVE is highlighted by a red box.  $\Delta x_i(0)$  and  $\Delta x_i$ ,  $i = 1, 2, 3$ , are the edge length of the red box in the  $i$  direction for undeformed and buckled crystals, respectively. c) Magnified views of the inner-most RVE taken from micro-CT X-ray scanning at different levels of strains. d) Corresponding pictures taken from simulation. (Green scale bars: 20 mm).

deformed Bucklicrystal bend inwards, a clear indication of a 3D negative Poisson's ratio.

Recognizing that the response of the specimens is necessarily influenced by boundary conditions at both the loaded and the traction-free faces, we focused on the inner-most building block, which can be considered as the representative volume element (RVE) for the corresponding infinitely periodic structure, and quantitatively estimated its deformation using image post-processing. First, each tomographic image was size-calibrated using the known shell thickness ( $t = 7.1$  mm), which was only marginally affected by deformation. We then tracked the centroids of the four voids surrounding the RVE in both the 1–2 and the 2–3 planes (see vertices of the red rectangle in Figures 2a,b) and used them to calculate centroid-to-centroid distances along the three directions, denoted by  $\Delta x_1$ ,  $\Delta x_2$ , and  $\Delta x_3$ . Prior to compression,

the value for all of these quantities was  $\Delta x_i(0) \approx 38$  mm,  $i = 1, 2, 3$ . Local normal strains were then obtained as  $\epsilon_{ii} = \langle \Delta x_i \rangle / \Delta x_i(0)$ , where the angular bracket  $\langle \rangle$  denotes ensemble average over all distances under consideration. It is worth noting that the measured local longitudinal strains, denoted by  $\epsilon_{22}$ , were higher than those applied, denoted by  $\epsilon_{22}^{\text{applied}}$ . This was expected since the building blocks in close proximity of the two plates used to compress the structure were highly constrained by friction and were unable to fully deform.

In Figure 3a, we present the dependence of the transverse strains  $\epsilon_{11}$  and  $\epsilon_{33}$  on the longitudinal strain  $\epsilon_{22}$ . The error bars on the experimental points were obtained from the standard deviation of the two values of  $\Delta x_i$  used in each averaging. Remarkably, the data clearly show that upon increasing the compressive strain  $\epsilon_{22}$ , both transverse strains decrease,

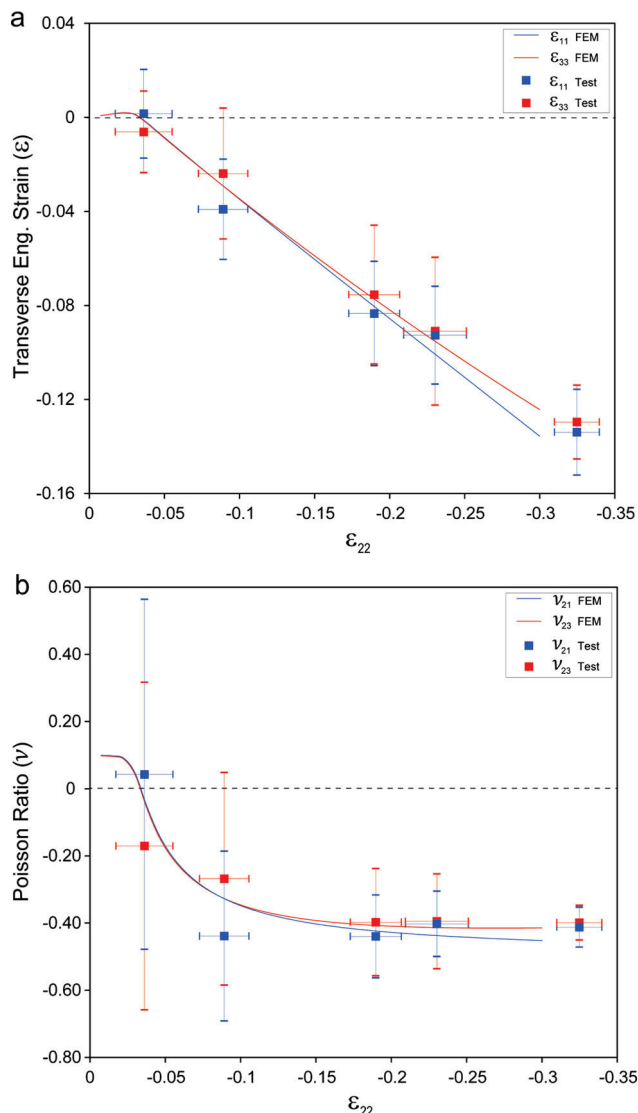


**Figure 3.** Evolution of transverse strains and Poisson's ratios for the 6-hole Bucklicrystal. a) Evolution of the transverse engineering strain  $\epsilon_{11}$  and  $\epsilon_{33}$  as a function of the applied longitudinal strain  $\epsilon_{22}$ . b) Evolution of the Poisson's ratios ( $\nu_{21}$  and  $\nu_{23}$ ) of the 6-hole Bucklicrystal as a function of compressive strain  $\epsilon_{22}$ . The finite element results (solid lines) are in good agreement with the experimental data (square markers).

indicating that the structure contracts in both lateral directions. To quantify these lateral contractions, the Poisson's ratios were calculated from the engineering strain as  $\nu_{ij} = -\epsilon_{ii}/\epsilon_{jj}$ . The estimates of  $\nu_{ij}$  were plotted as a function of  $\epsilon_{22}$  in Figure 3b. The evolution of  $\nu_{21}$  and  $\nu_{23}$  was characterized by two subsequent regimes: a decreasing regime followed by a plateau. Initially both Poisson's ratios monotonically decrease. They became negative at  $\epsilon_{22} \approx -0.03$ , and eventually reached the value  $\nu \approx -0.4$  and plateau at  $\epsilon_{22} \approx -0.20$ , demonstrating that the response of the Bucklicrystal was auxetic over a wide range of deformations. Finally we note that, since the specimens are made of an elastomeric material, the process was fully reversible and repeatable. Upon release of the applied vertical displacement, the deformed structures recovered their original configurations.

Next, we performed finite element (FE) simulations of the 6-hole Bucklicrystal. To verify that the auxetic behavior measured in the experiments was not affected by the boundary conditions, we considered the structure to be infinite and investigated the response of the RVE under uniaxial compression using periodic boundary conditions. All analyses were performed on the cubic RVE comprising a central building block connected to one-eighth of the building block at each junction (the junctions and the RVE are shown in Figure 1a).

We first investigated the stability of the Bucklicrystal through Bloch wave analysis<sup>[18,19]</sup> and the analysis detected a mechanical instability at  $\epsilon_{22} = -0.03$ . The post-buckling response of the Bucklicrystal was then simulated by introducing a small imperfection in the initial geometry. In Figure 2d, we present a sequence of the progressive collapse of the Bucklicrystal obtained from FE simulations, which is in remarkable qualitative agreement with the experiments for the same geometric and material parameters (Figure 2c). The snapshots clearly revealed that in this Bucklicrystal, mechanical instabilities act as a functional mode of actuation, inducing the spherical collapse of every building block while keeping the structure periodic. To better characterize the response of the structure, in Figure 3 we report the evolution of the lateral strains ( $\epsilon_{11}$ ,  $\epsilon_{33}$ ) and Poisson's ratios ( $\nu_{21}$ ,  $\nu_{23}$ ) as a function of  $\epsilon_{22}$ , showing an excellent quantitative agreement with our experimental results. It is worth noting that, since after buckling the initial cubic RVE changes into a rectangular parallelepiped, for large values of longitudinal strain  $\epsilon_{33} \neq \epsilon_{11}$  and  $\nu_{21} \neq \nu_{23}$ . This can be clearly seen in Figure 2d for  $\epsilon_{22}^{\text{applied}} = -0.30$ , where all of the ligaments in the 1–2 plane are touching, while in the 2–3 plane, they are still separated from each other.

Given the excellent qualitative and quantitative agreement found between our experiments and simulations, we proceeded by focusing primarily on the FE simulation results to further explore the buckling-induced auxetic behavior of all the Bucklicrystals identified in Figure 1. Each building block is fully characterized by two adimensional parameters: porosity, denoted by  $\psi$ , (defined as the ratio of the void volume to the intact spherical shell volume) and thickness over inner radius ratio, denoted by  $t/r_1$ .<sup>[17]</sup> All crystals were constructed using building blocks characterized by the same parameters used for the 6-hole crystal investigated above,  $\psi = 0.733$  and  $t/r_1 = 5/7$ .

All analyses were performed on cubic RVEs (Figures 1b and S2): (i) for *bcc* configurations (12- and 24-hole), they were constructed as described for the 6-hole *bcc* case; (ii) for the *sc* configurations (12- and 24-hole), a single building block was used as RVEs; (iii) for the *fcc* configuration (24-hole), RVEs were built such that they comprise of 6 half-building blocks located in the middle of the cube faces, attaching to 8 one-eighth of the building blocks at the corners. It is worth noting that the use of building blocks characterized by the same parameters  $\psi$  and  $t/r_1$  resulted in Bucklicrystals with different initial global porosities, denoted by  $\bar{\psi}$  (i.e.  $\bar{\psi}_{sc} = 0.888$ ,  $\bar{\psi}_{bcc} = 0.854$  and  $\bar{\psi}_{fcc} = 0.842$ ). In all Bucklicrystals, instabilities of short wavelength were found to be critical, leading to spherical collapse of all the building blocks. The values of critical strain obtained from Bloch wave analysis were  $\epsilon_{22}^{\text{cr}} = -0.030$ ,  $-0.030$ ,  $-0.041$ ,  $-0.020$ ,  $-0.026$ , and  $-0.023$  for 6-hole *bcc*, 12-hole *bcc* and *sc*, and 24-hole *bcc*, *sc* and *fcc*, respectively. Moreover, the deformed

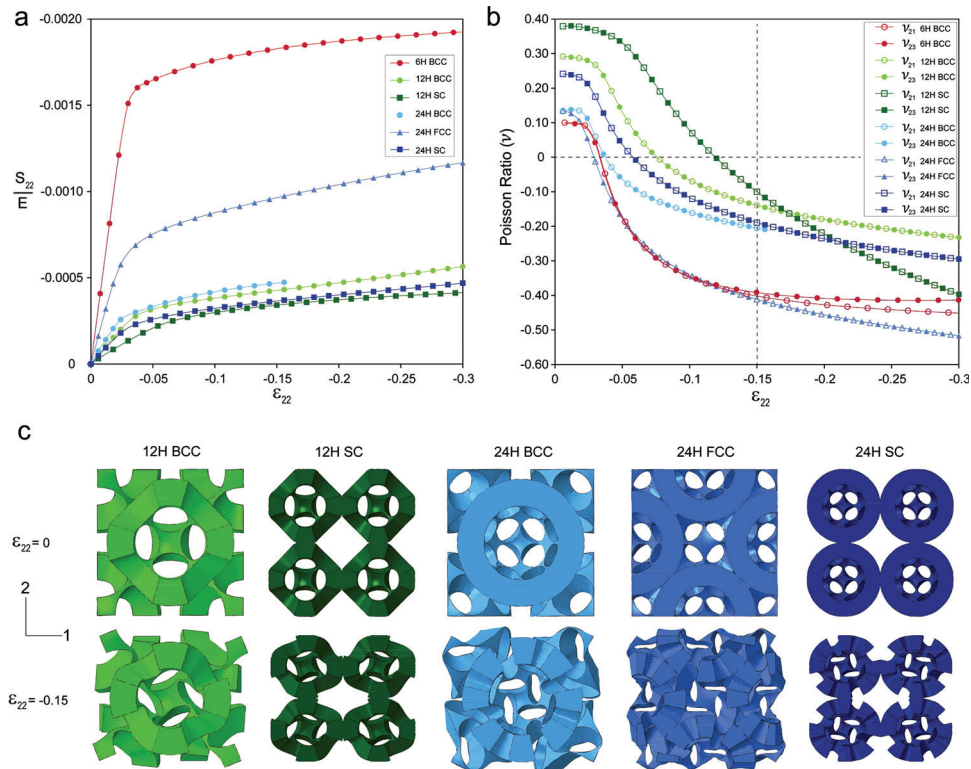


**Figure 4.** Mechanical response of Bucklicrystals. a) Nominal stress-strain curves from uniaxial compression in 2-direction for all of the Bucklicrystals. The stress is normalized with respect to the elastic modulus of the bulk elastomeric material. b) Evolution of the Poisson's ratios vs. nominal strain in 2-direction for all the Bucklicrystals. c) Cross sectional views of undeformed ( $\epsilon_{22} = 0$ ) and deformed ( $\epsilon_{22} = -0.15$ ) configurations of 12- and 24-hole Bucklicrystals.

mode shapes of the RVEs are reported in Figure 1c. Note that for the *sc* configurations, when the critical instability occurs, the periodicity of the crystal was altered and a new RVE comprised of 8 building blocks was found (RVE size =  $2 \times 2 \times 2$  in 1, 2, and 3 directions). Furthermore, in the building blocks with 12 or 24 holes, the identical junctions (i.e. the sites where adjacent building blocks can be attached to each other) rotate all in the same direction during folding (Figure S6). As a result, in Bucklicrystals comprising arrays of building blocks with 12 or 24 holes, the folded units have two potentially different orientations (Figure S7). In contrast, in the 6-hole building block, half of the junctions rotate clockwise and half counterclockwise (Figure S6). As a result, in the deformed configuration of the 6-hole *bcc* Bucklicrystal, all of the folded building blocks are oriented in exactly the same way (Figure S8).

A more quantitative comparison between the responses of all of the Bucklicrystals can be made by inspecting the evolution of stresses and Poisson's ratios. Figure 4 shows the evolution of the normalized nominal stress  $S_{22}/E$  as a function of the longitudinal strain  $\epsilon_{22}$ . The response of all configurations is characterized by a linear elastic regime followed by a stress plateau. The departure from linearity is the result of buckling and corresponds to a sudden transformation in the periodic pattern as shown in Figure 4c, where snapshots of undeformed and deformed ( $\epsilon_{22} = -0.15$ ) configurations are presented. Note that all of the crystals are uniaxially compressed up to the limit when the ligaments surrounding the holes begin to contact one

another. This results in a maximum longitudinal strain  $\epsilon_{22} \approx -0.30$  for all the crystals, except the *bcc* crystal comprising of an array of 24-hole building blocks in which the ligaments come into contact with each other at  $\epsilon_{22} \approx -0.15$ . Finally, it is worth noting that all the structures exhibit a typical behavior for cellular solids characterized by an initial linear elastic regime and a stress plateau following thereafter. The final steep portion of the curve (i.e. densification) is not observed since the applied strain is not large enough to completely collapse the holes.

The evolution of the Poisson's ratios as a function of  $\epsilon_{22}$  is also presented in Figure 4b. All of the Bucklicrystals are characterized by initial positive values of  $\nu$ , a steeply decreasing regime initiated at the onset of instability, and a final negative plateau by further compression. Therefore, in all the Bucklicrystals, an evolution of the Poisson's ratio from positive to negative is observed; this transition occurs first in the 24-hole *fcc* Bucklicrystal (at  $\epsilon_{22} \approx -0.04$ ) and last in the 12-hole *sc* (at  $\epsilon_{22} \approx -0.12$ ). Remarkably, once the crystals become auxetic, they retain this unusual property even at large strains. At  $\epsilon_{22} = -0.30$ , all configurations are characterized by negative Poisson's ratio, ranging from  $-0.2$  for the 12-hole *bcc* crystal to  $-0.5$  for the 24-hole *fcc*. Finally, we note that all the crystals, except the 6-hole case, retain the transversely symmetric behavior (i.e.  $\nu_{21} = \nu_{23}$ ) even at large strains.

Our finding of buckling-induced auxetic behavior provides a fundamentally new way for generating 3D materials with a negative Poisson's ratio. Our results offer a unique mechanism

with a range of advantages: (i) the proposed design rules can be applied to various length-scales; (ii) the reconfiguration can occur upon application of different stimuli depending on the types of materials; (iii) the transformation can be made fully reversible; and (iv) the auxetic behavior is retained over a wide range of applied strain. While the fabrication process described here is not tractable for the large scale production of these materials, it provides an effective proof of concept method to construct various models and evaluate their mechanical performance. Based on these initial observations, we are currently developing large-scale 3D-printed sacrificial molds from soluble materials which would allow the bucklicrystals to be cast in a single step process. This new approach reduces the production time of these materials by more than 90% and permits the exploration of more complex geometries. From a practical perspective, the full control over the desired outcome in combination with the wealth of different length scales, materials, stimuli, and geometrical designs provides reversibly auxetic architectures with a broad field of applications ranging from energy absorbing materials to tunable membrane filters. Finally, although mechanical instabilities have been traditionally viewed as a failure mode with research focusing on how to avoid them, here we change this perspective and exploit instabilities to design a new class of 3D auxetic materials.

## Experimental Section

**Materials:** A silicone-based rubber (commercial name: Elite Double 32, Zhermack) was used to cast the experimental specimen. The material properties were measured through tensile testing, up to the true strain of  $\varepsilon = 0.60$ . No hysteresis was found during loading and unloading. The constitutive behavior was accurately captured by a Yeoh hyperelastic model,<sup>[20]</sup> whose strain energy is  $U = \sum_{i=1}^3 C_{i0}(\bar{I}_1 - 3)^i + (J - 1)^2/D_i$  where  $C_{10} = 131$  KPa,  $C_{20} = 0$  KPa,  $C_{30} = 3.5$  Kpa,  $D_1 = D_2 = D_3 = 154$  GPa<sup>-1</sup>. Here,  $\bar{I}_1 = \text{tr}[\text{dev}(\mathbf{F}^T \mathbf{F})]$ ,  $J = \det(\mathbf{F})$ , and  $\mathbf{F}$  is the deformation gradient. Two of the Yeoh model parameters are related to the conventional shear modulus, denoted by  $G_0$ , and bulk modulus, denoted by  $K_0$ , at zero strain:  $C_{10} = G_0/2$ ,  $D_1 = 2/K_0$ .

**Fabrication of the building blocks:** A mold was fabricated using a 3D printer (Objet Connex500) to cast one half of a spherical shell. After de-molding, two halves were joined using the same polymer as adhesive agent. The specimen fabricated for this study has the thickness of  $t = 7.1$  mm, the inner diameter of  $d_i = 19.8$  mm, and the outer diameter of  $d_o = 34.0$  mm.

**Testing of the Bucklicrystal:** After preparing 91 spherical shells, all the shells were joined using the same polymer as adhesive agent. The dimension of the Bucklicrystal was Height  $\times$  Width  $\times$  Depth =  $144.0 \times 141.0 \times 141.0$  mm. In order to observe the evolution of the Poisson's ratio of the Bucklicrystal, we applied five different levels of vertical deformation, i.e. engineering strains of  $\varepsilon_{22} = -0.03, -0.08, -0.15, -0.20$  and  $-0.30$  with respect to the height of the Bucklicrystal. At the strain level of interest, we immobilized the specimen using a fixture made of acrylic plates, nylon bolts/nuts and inch-thick closed-cell foam plates placed between the specimen and the fixture (Figure S3). The foam plates were used as a low electron density spacer that would be nearly invisible in the acquired x-ray transmission images and thus not interfere with volume rendering of the higher electron density silicone elastomer Bucklicrystal. The specimen with the fixture was put into a micro-CT X-ray scanner (HMXST225, X-Tek) for image data collection. Once the 3D volumes of the inside of the specimen were reconstructed, the cross-sectional views of interest were extracted.

**Numerical Simulations:** The simulations were carried out using the commercial Finite Element package Abaqus (SIMULIA, Providence, RI).

The Abaqus/Standard solver was employed for all the simulations, i.e., for both microscopic and macroscopic instability analyses and post-buckling analysis. Models were built using quadratic solid elements (Abaqus element type C3D10M with a mesh sweeping seed size of 1 mm) and the analyses were performed under uniaxial compression. We used first four eigenvalues from instability analysis as imperfection on non-linear post Buckling analysis. More details on the FE simulations are provided in the Supporting Information.

## Supporting Information

Supporting Information is available from the Wiley Online Library or from the author.

## Acknowledgements

This work has been supported by Harvard MRSEC through grant DMR-0820484, by NSF through grant CMMI-1149456 (CAREER) and by the Wyss Institute through the Seed Grant Program. K.B. acknowledges start-up funds from the Harvard School of Engineering and Applied Sciences. E.R.C. acknowledges NSF MSPRF grant DMS-1204686. This work was performed in part at the Center for Nanoscale Systems (CNS), a member of the National Nanotechnology Infrastructure Network (NNIN), which is supported by the National Science Foundation under NSF award no. ECS-0335765. CNS is part of Harvard University.

Received: May 2, 2013

Revised: June 4, 2013

Published online:

- [1] J. Pendry, a. J. Holden, D. Robbins, W. Stewart, *IEEE Transactions on Microwave Theory and Techniques* **1999**, *47*, 2075.
- [2] C. M. Soukoulis, M. Wegener, *Nat. Photonics* **2011**, *5*, 523.
- [3] M. H. Lu, L. Feng, Y. F. Chen, *Mater. Today* **2009**, *12*, 34.
- [4] J. H. Lee, J. P. Singer, E. L. Thomas, *Adv. Mater.* **2012**, *24*, 4782.
- [5] G. N. Greaves, A. Greer, R. Lakes, T. Rouxel, *Nat. Mater.* **2011**, *10*, 823.
- [6] R. Lakes, *Adv. Mater.* **1993**, *5*, 293.
- [7] K. E. Evans, A. Alderson, *Adv. Mater.* **2000**, *12*, 617.
- [8] R. Lakes, *Science* **1987**, *235*, 1035.
- [9] Y. Liu, H. Hu, *Sci. Res. Essays* **2010**, *5*, 1052.
- [10] R. H. Baughman, J. M. Shacklette, A. A. Zakhidov, S. Stafstro, *Nature* **1998**, *392*, 362.
- [11] T. Hughes, A. Marmier, K. Evans, *Int. J. Solids Struct.* **2010**, *47*, 1469.
- [12] P. V. Pikhitsa, M. Choi, H. J. Kim, S. H. Ahn, *Phys. Status Solidi (B)* **2009**, *246*, 2098.
- [13] D. Attard, J. N. Grima, *Phys. Status Solidi (B)* **2009**, *249*, 1330.
- [14] T. Bückmann, N. Stenger, M. Kadic, J. Kaschke, A. Frölich, T. Kennerknecht, C. Eber, M. Thiel, M. Wegener, *Adv. Mater.* **2012**, *24*, 2710.
- [15] A. Sidorenko, T. Krupenkin, A. Taylor, P. Fratzl, J. Aizenberg, *Science* **2007**, *315*, 487.
- [16] K. Bertoldi, P. M. Reis, S. Willshaw, T. Mullin, *Adv. Mater.* **2010**, *22*, 361.
- [17] J. Shim, C. Perdigou, E. R. Chen, K. Bertoldi, P. M. Reis, *Proc. Natl. Acad. Sci. USA* **2012**, *109*, 5978.
- [18] K. Bertoldi, M. Boyce, S. Deschanel, S. Prange, T. Mullin, *J. Mech. Phys. and Solids* **2008**, *56*, 2642.
- [19] G. Geymonat, S. Muller, N. Triantafyllidis, *Arch. Rational Mech. Anal.* **1993**, *122*, 231.
- [20] O. Yeoh, *Rubber Chem. Technol.* **1993**, *66*, 754.

# ADVANCED MATERIALS

## Supporting Information

for *Adv. Mater.*, DOI: 10.1002/adma.201301986

3D Soft Metamaterials with Negative Poisson's Ratio

*Sahab Babaee , Jongmin Shim , James C. Weaver , Elizabeth R. Chen , Nikita Patel , and Katia Bertoldi \**

Supplementary Material for  
3-D Soft Metamaterials with Negative Poisson's Ratio

Sahab Babae<sup>\*,1</sup>, Jongmin Shim<sup>\*\*,1</sup>, James C. Weaver<sup>+</sup>, Elizabeth R. Chen<sup>\*</sup>, Nikita Patel<sup>\*</sup>, and Katia Bertoldi<sup>\*,2</sup>

<sup>\*</sup>*School of Engineering and Applied Science, Harvard University, Cambridge, MA 02138*

<sup>+</sup>*Wyss Institute for Biologically Inspired Engineering, Harvard University, Cambridge, MA 02138*

<sup>1</sup>*Contributed equally to this work*

<sup>2</sup>*Kavli Institute, Harvard University, Cambridge, MA 02138*

<sup>\*\*</sup>*Department of Civil, Structural and Environmental Engineering, University at Buffalo, Buffalo, NY*

14260

## S1 Building blocks

The building blocks for all the proposed metamaterials are patterned spherical shells [1], in which a significant change in volume is observed as a result of elastic instabilities. Since here we focus on cubic crystal systems and require both the building blocks and the metamaterial to have octahedral symmetry, only patterned spherical shells with 6, 12 and 24 holes are considered. Different views of the three building blocks discussed in this study are shown in Fig. S1.

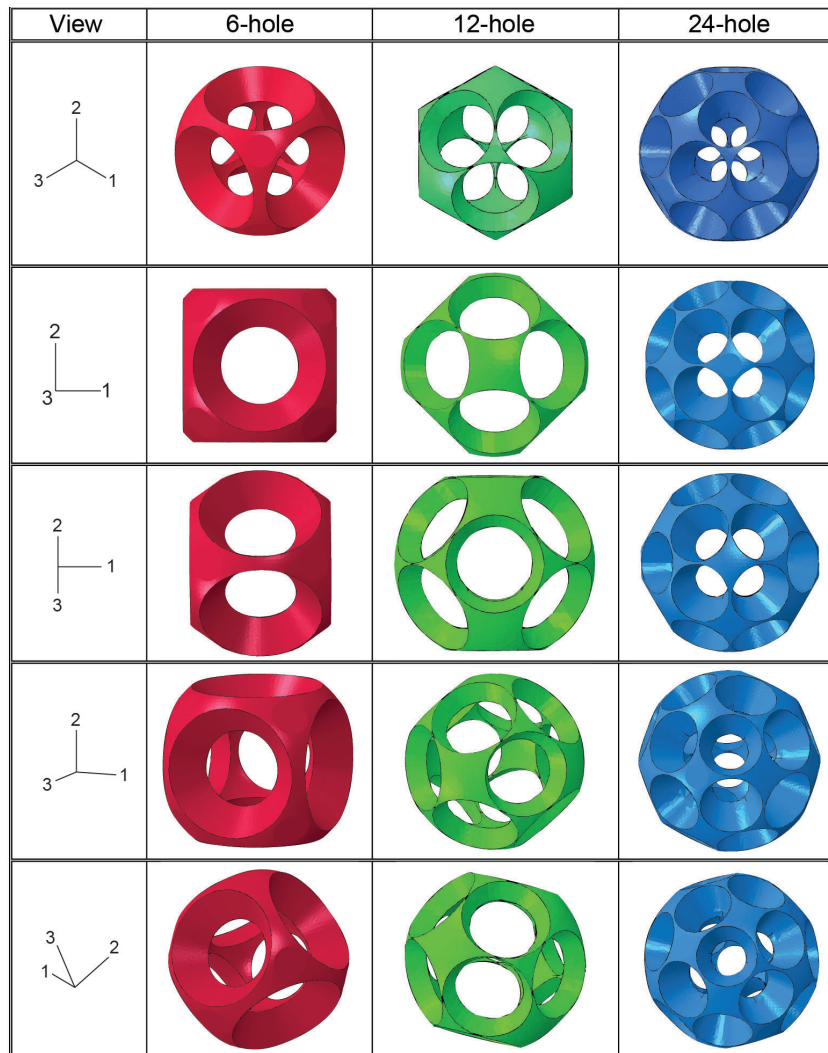


Figure S1: Different views of the building blocks with 6, 12, and 24 holes.

## S2 Representative Volume Elements

Since each building block has a limited number of sites where adjacent building blocks can be attached to each other and metamaterials with octahedral symmetry can only be built through connecting identical junctions, only six different Bucklicrystals can be built: *bcc* crystals using building blocks with 6, 12 or 24 holes, *sc* crystals using building blocks with 12 or 24 holes and *fcc* crystal using building blocks with 24 holes. Different views of the representative volume elements (RVEs) for each metamaterial in the undeformed configuration are shown in Fig. S2.

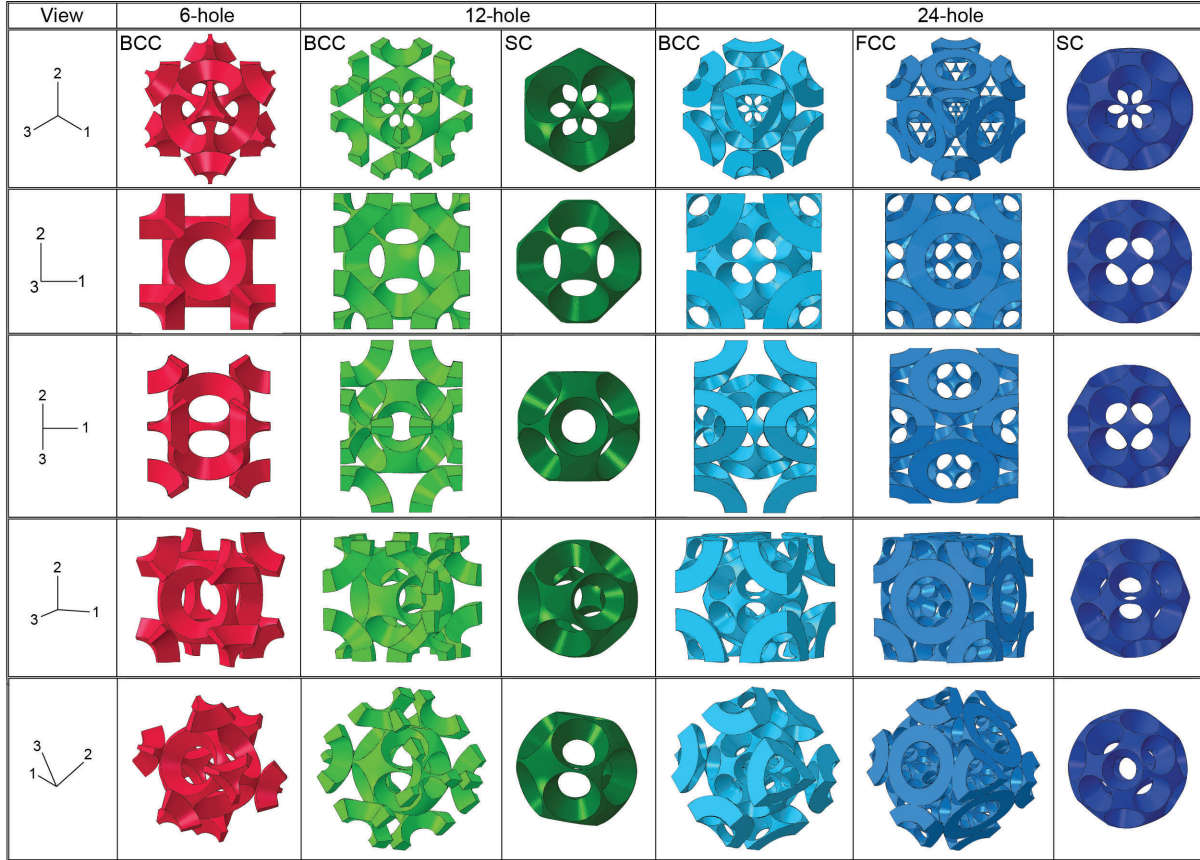


Figure S2: Different views of the undeformed RVEs for all the proposed Bucklicrystals.

### S3 Experiments

To monitor the evolution of the Poisson's ratio of the fabricated Bucklicrystal, we tested the structure under uniaxial compression. At the strain level of interest, we immobilized the specimen using a fixture made of acrylic plates, nylon bolts/nuts and inch-thick closed-cell foam plates placed between the specimen and the fixture (see Fig. S3). The foam plates were used as a low electron density spacer that would be nearly invisible in the acquired x-ray transmission images and thus not interfere with volume rendering of the higher electron density silicone elastomer Bucklicrystal.

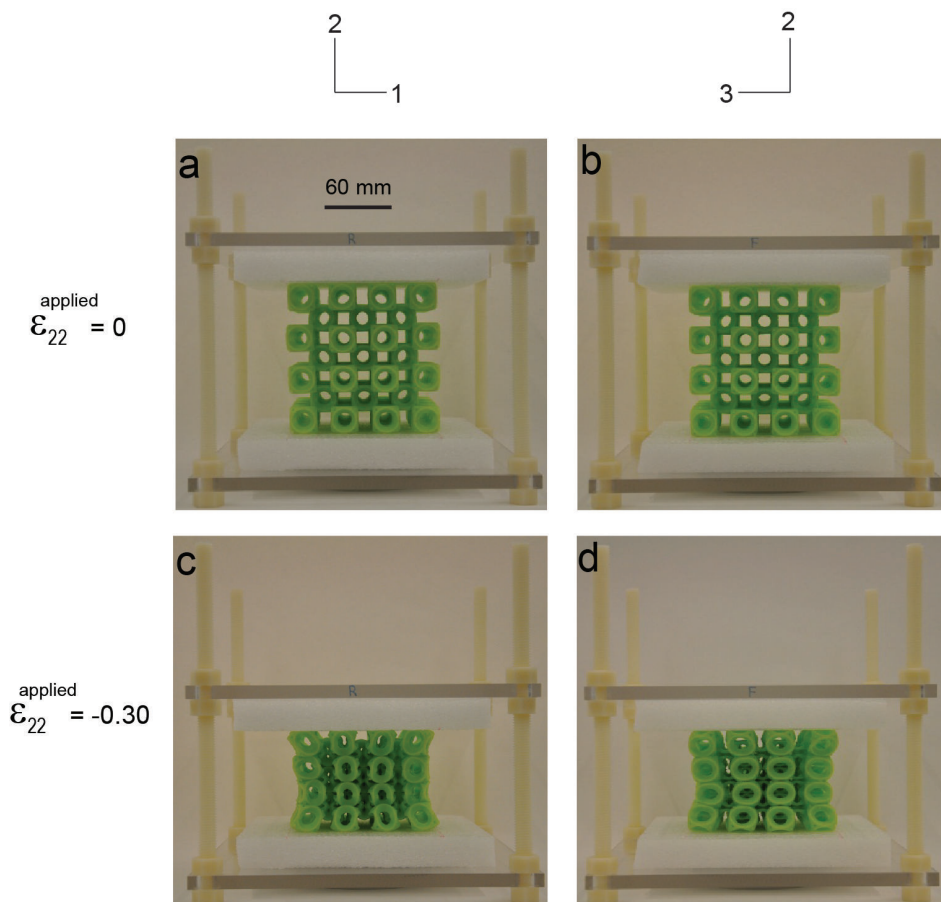


Figure S3: **Testing of the Bucklicrystal.** a,b, Undeformed configuration. c,d, Deformed configuration at  $\epsilon_{22}^{\text{applied}} = -0.3$ . (scale bar: 60mm)

## S4 Numerical simulations of stability analysis for 3D periodic structures

We investigated the buckling of 3D periodic porous structures using non-linear finite element (FE) analyses. The FE calculations were conducted within the nonlinear code ABAQUS, version 6.8-2. In the numerical analyses, we investigated the stability of infinitely periodic structures comprising of an array of perfectly connected building blocks. For the sake of computational efficiency, the analyses were conducted on representative volume elements (RVEs) (see Fig. S2).

For infinite periodic structures, it is useful to make the distinction between *microscopic* instabilities (i.e. instabilities with wavelengths that are of the order of the size of the microstructure) and *macroscopic* instabilities (i.e. instabilities with much larger wavelengths in comparison to the size of the unit cell) [2–5].

**Microscopic instabilities.** Although microscopic (local) buckling modes may alter the initial periodicity of the solid, they can still be detected by studying the response of a single unit cell and investigating the propagation of small-amplitude waves with an arbitrary wave vector superimposed on the current state of deformation [2–4]. While a real angular frequency  $\omega$  corresponds to a propagating wave, a complex  $\omega$  identifies a perturbation exponentially growing with time. Therefore, the transition between stable and unstable configurations is detected when the frequency vanishes (i.e.  $\omega = 0$ ) and the new periodicity of the solid introduced by instability can be easily obtained by the corresponding wave vector. Here, the finite-element method was used to perform the Bloch wave analysis [4].

**Macroscopic instabilities.** Following Geymonat et al. [2], we examined macroscopic instabilities by detecting the loss of strong ellipticity of the overall response of the periodic structure. Specifically, for the metamaterials considered in this study macroscopic instabilities may occur whenever the condition

$$\mathbb{L}_{ijkl}^H N_j N_l m_i m_k > 0 \quad \text{for} \quad \mathbf{m} \otimes \mathbf{N} \neq 0, \quad (\text{S1})$$

is first violated along the loading path,  $\mathbb{L}^H$  being the macroscopic (homogenized) tangent modulus and  $\mathbf{N}$  and  $\mathbf{m}$  denoting unit vectors. Note that  $\mathbb{L}^H$  is evaluated numerically by subjecting the RVE to nine independent linear perturbations of the macroscopic deformation gradient [4].

## S5 Stability analysis for the 6-hole Bucklicrystal

We started by investigating the stability of the 6-hole Bucklicrystal. For the considered periodic structure, the onsets of both microscopic and macroscopic instabilities were detected by studying the response of the RVE depicted in Fig. S4-left. A microscopic instability was detected at  $\epsilon_{22} = -0.03$ , while the onset of macroscopic instability occurs at  $\epsilon_{22} = -0.06$ . Therefore, microscopic instabilities were always critical in compression, leading to a critical mode where all building blocks underwent the same rotation (see Figs. S4-right), without altering the structure's periodicity.

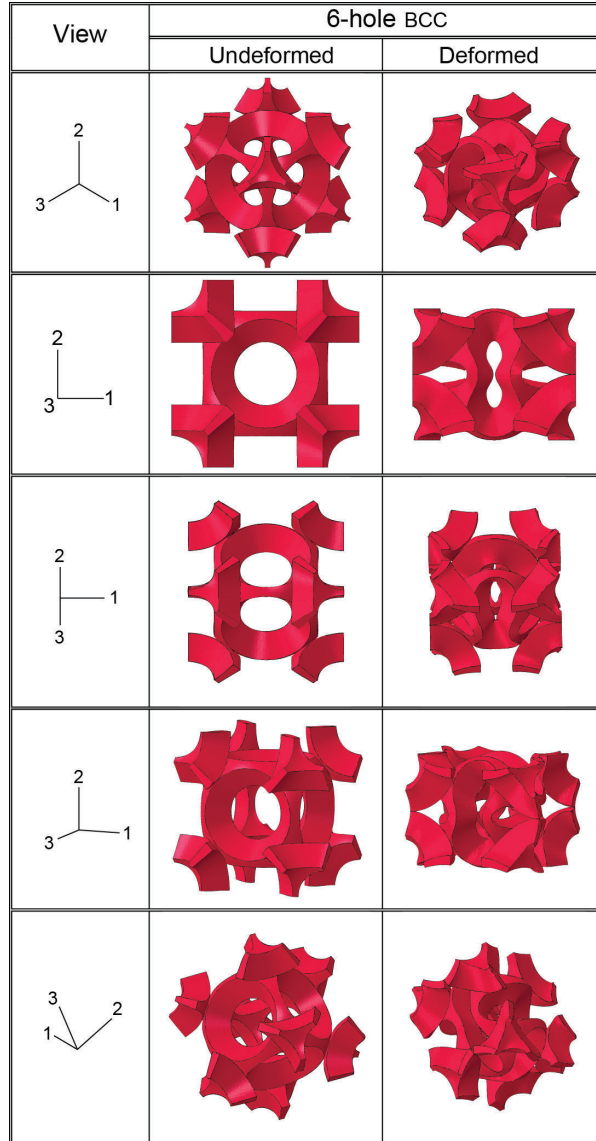


Figure S4: Left: RVE for the undeformed 6-hole *bcc*. Right: Critical mode detected by the Bloch wave analysis. Note that the deformation of the RVE is slightly different in 1 and 3 directions.

## S6 Stability analysis for all Bucklicrystals

The onsets of both microscopic and macroscopic instabilities for each Bucklicrystal was detected by studying the response of the RVEs depicted in Fig. S2. In all Bucklicrystals, instabilities of short wavelength were found to be critical, leading to spherical collapse of all the building blocks. The values of critical strain obtained from the stability analysis are summarized in Table S1 and the corresponding critical modes are shown in Fig. S5. Note that for *sc* configurations, buckling leads to an enlarged RVE comprising of 8 building blocks (RVE size =  $2 \times 2 \times 2$  in 1, 2, and 3 directions). Moreover, it is worth noting that the non-linear deformation of the Bucklicrystals is dictated by the folding mechanism of the corresponding building blocks. Interestingly, in the Buckliball with 12 or 24 holes, all the junctions (*i.e.* the sites where adjacent building blocks can be attached to each other) rotate all in the same direction during folding (Fig. S6). As a result, in Bucklicrystals comprising arrays of building blocks with 12 or 24 holes, the folded units have two potentially different orientations (Fig. S7). In contrast, in the 6-hole Buckliball, half of the junctions rotate clockwise and half counterclockwise (Fig. S6). As a result, in the deformed configuration of the 6-hole *bcc* Bucklicrystal, all of the folded building blocks are oriented exactly in the same way (Fig. S8).

	$\epsilon_{22}^{micro}$	$\epsilon_{22}^{macro}$
6H-bcc	-0.030	-0.060
12H - bcc	-0.030	-0.140
12H- sc	-0.041	-0.265
24H-bcc	-0.020	-0.062
24H-sc	-0.026	-0.096
24H-fcc	-0.023	-0.050

Table S1: Values of critical strain for microscopic ( $\epsilon_{22}^{micro}$ ) and macroscopic ( $\epsilon_{22}^{macro}$ ) instabilities.

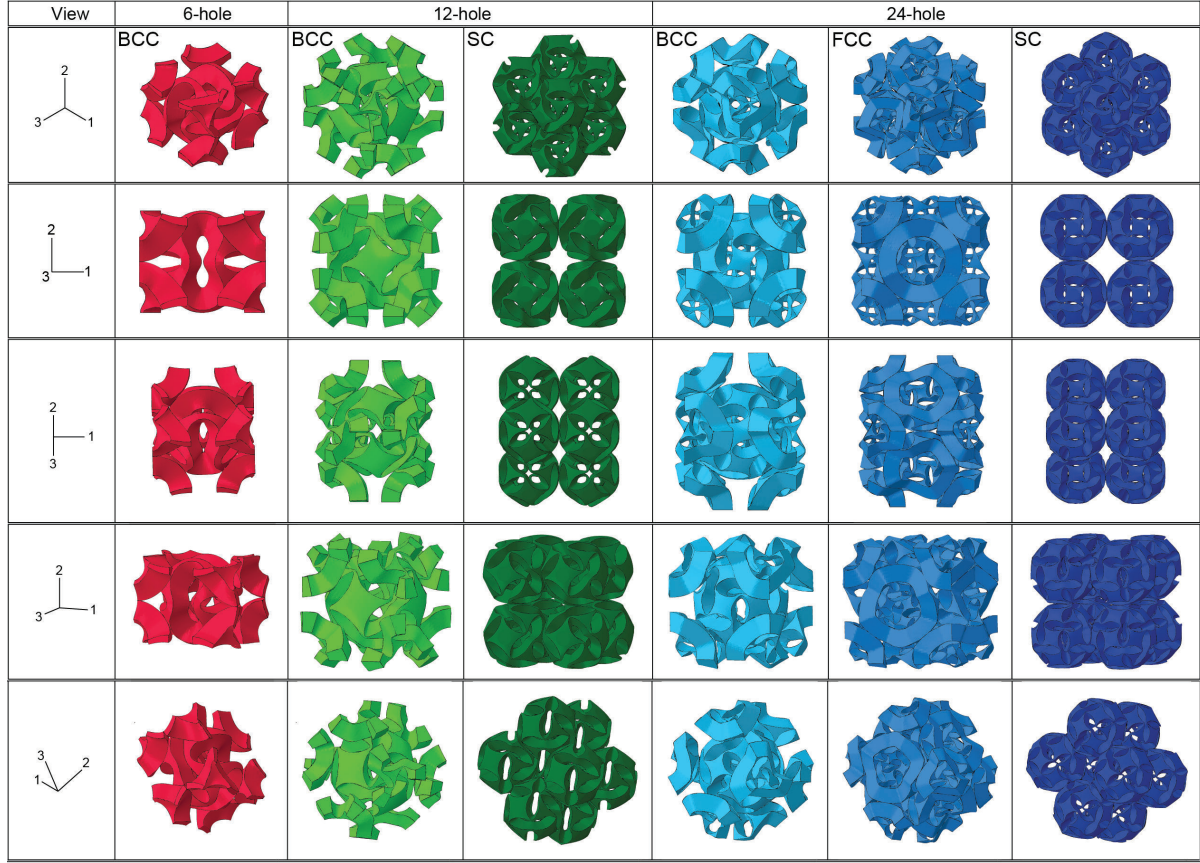


Figure S5: **Critical modes for all the Bucklicrystals under uniaxial compression.** Upon applying a load in the 2- direction, all the ligaments undergo the first buckling mode and all the circular holes close uniformly. Note that for *sc* configurations, buckling leads to an enlarged RVE, which is comprised of 8 building blocks (RVE size =  $2 \times 2 \times 2$  in 1, 2, and 3 directions).

## S7 Porosity of the Bucklicrystals

Each building block is fully characterized by two adimensional parameters: porosity, denoted by  $\psi$ , and thickness over inner radius ratio, denoted by  $t/r_i$  [1]. The porosity of a single building block is defined as a ratio of volume of the voids to volume of the intact shell [1]

$$\psi = \frac{V_{voids}}{V_{intact\ shell}}, \quad (S2)$$

where

$$V_{intact\ shell} = \frac{4}{3}\pi(r_o^3 - r_i^3), \quad (S3)$$

$r_i$  and  $r_o$  denoting the inner and outer radius of the spherical shell, respectively. The volume fraction of the structured shell is then simply defined as

$$V_{shell} = (1 - \psi)\frac{4}{3}\pi(r_o^3 - r_i^3). \quad (S4)$$

In this study all crystals are constructed using building blocks characterized by  $\psi = 0.733$  and  $(r_o - r_i)/r_i = 5/7$ . It is important to note that the use of building blocks characterized by

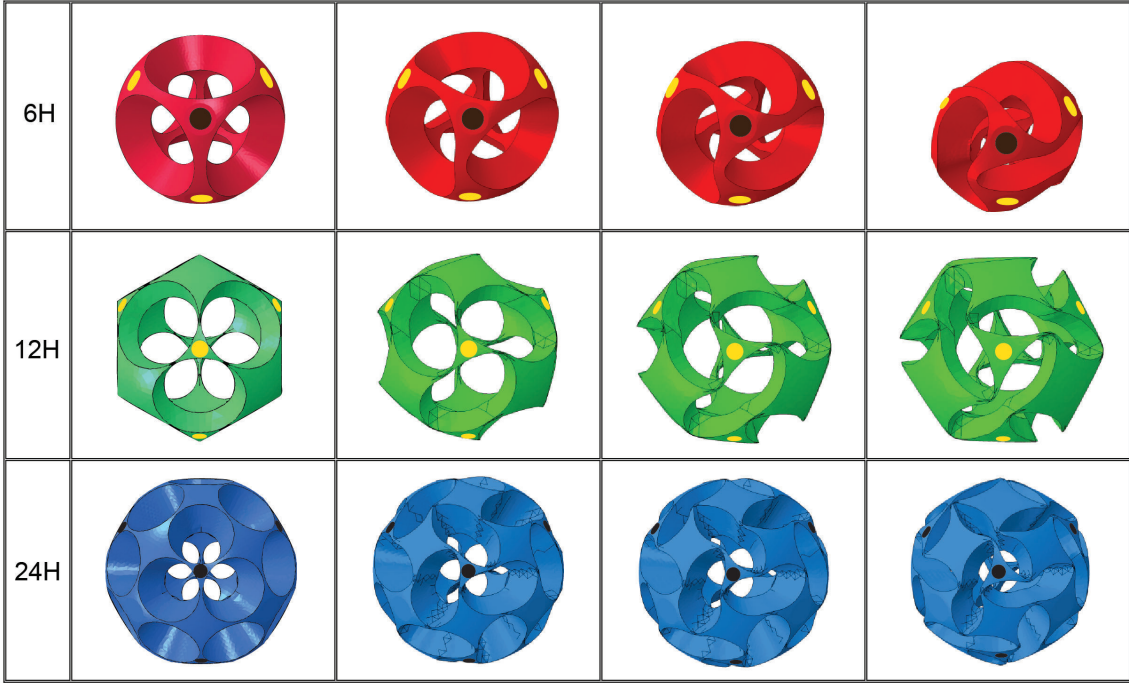


Figure S6: **Sequence of progressively deformed configurations of the building blocks.** The circular markers are used to highlight the rotation of the junctions used to build *bcc* Bucklicrystals. Yellow markers indicate a counterclockwise rotation, while black markers correspond to a clockwise rotation. In the 6-hole building block, half of the junctions rotate clockwise and half counterclockwise, as indicated by the yellow and black markers. In contrast, for the building block with 12 or 24 holes, all identical junctions rotate in the same direction.

the same parameters  $\psi$  and  $t/r_i$  results in Bucklicrystals with different initial global porosities  $\bar{\psi}$ .

The global porosity for each packing configurations (*sc*, *bcc*, and *fcc*) is defined as

$$\bar{\psi} = 1 - \frac{N_{\text{building block}} V_{\text{shell}}}{V_{\text{RVE}}}, \quad (\text{S5})$$

where  $N_{\text{building block}}$  is the number of building blocks in the RVE and  $V_{\text{RVE}} = L^3$  is the volume of the cubic RVE of length  $L$ . Note that each packing configuration is characterized by a unique pair  $\langle N_{\text{building block}}, L \rangle$ . More specifically,  $\langle N_{\text{building block}}, L \rangle = \langle 1, 2r_0 \rangle$ ,  $\langle 2, \frac{4r_0}{\sqrt{3}} \rangle$ , and  $\langle 4, \frac{4r_0}{\sqrt{2}} \rangle$  for *sc*, *bcc*, and *fcc* packing configurations, respectively. Combining Eqs. (S4) and (S5), the global void volume fraction for Bucklicrystals characterized by  $\psi = 0.733$  and  $(r_o - r_i)/r_i = 5/7$  can be calculated as:  $\bar{\psi}_{sc} = 0.888$ ,  $\bar{\psi}_{bcc} = 0.854$  and  $\bar{\psi}_{fcc} = 0.842$ .

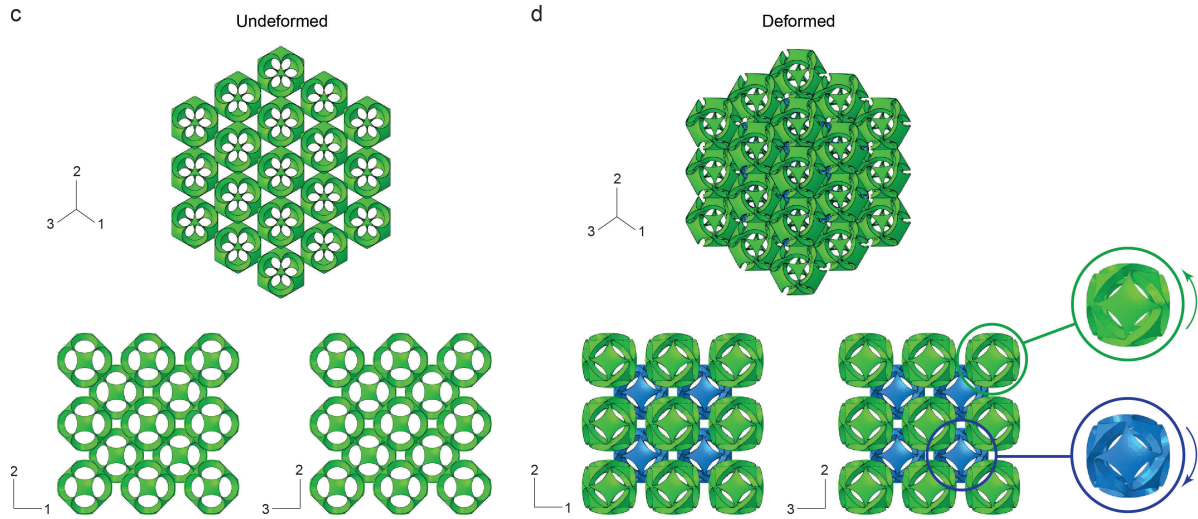


Figure S7: Left: Enlarged RVE for the undeformed 12-hole *bcc* comprising of 35 building blocks. Right: Reconstruction of the critical mode detected for the enlarged RVE. Note that the folded building blocks have two different orientations, as indicated by the two colors (blue and green). As a result, each unit is oriented differently with respect to the surrounding connected units.

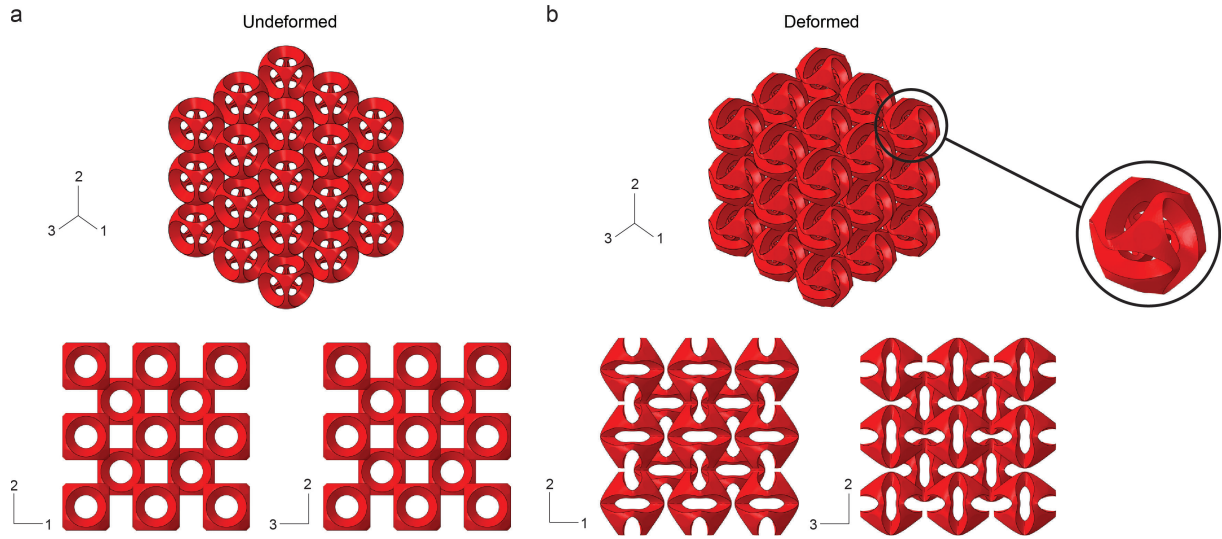


Figure S8: Left: Enlarged RVE for the undeformed 6-hole *bcc* comprising of 35 building blocks. Right: Reconstruction of the critical mode detected for the enlarged RVE. Note that all folded building blocks have exactly the same orientation.

## References

- [1] Shim J, Perdigou C, Chen ER, Bertoldi K, Reis PM (2012) Buckling-induced encapsulation of structured elastic shells under pressure. *Proceedings of the National Academy of Sciences of the United States of America* 109:5978–83.
- [2] Geymonat G, Muller S, Triantafyllidis N (1993) Homogenization of Nonlinearly Elastic Materials , Microscopic Bifurcation and Macroscopic Loss of Rank-One Convexity. *Arch. Rational Mech. Anal.* 122:231–290.
- [3] Triantafyllidis N, Nestorovic MD, Schraad MW (2006) Failure surfaces for finitely strained two-phase periodic solids under general in-plane loading. *Journal of Applied Mechanics* 73:505.
- [4] Bertoldi K, Boyce M, Deschanel S, Prange S, Mullin T (2008) Mechanics of deformation-triggered pattern transformations and superelastic behavior in periodic elastomeric structures. *Journal of the Mechanics and Physics of Solids* 56:2642–2668.
- [5] Overvelde JTB, Shan S BK (2012) Compaction through buckling in 2d periodic, soft and porous structures: Effect of pore shape. *Advanced Materials* 24:2337.